Nanomorphology of Eco-Friendly Colloidal Inks, Relating Non-Fullerene Acceptor Surface Energy to Structure Formation

Matthew G. Barr[1], Sylvain Chambon[2,3], Adam Fahy[1], Timothy W. Jones[4], Matthew A. Marcus[5], A. L. David Kilcoyne[5], Paul C. Dastoor[1], Matthew J. Griffith,[1,6] Natalie P. Holmes[1*]

[1] Centre for Organic Electronics, University of Newcastle, Callaghan, NSW 2308, Australia

[2] University of Bordeaux, IMS, CNRS, UMR 5218, Bordeaux INP, ENSCBP, F-33405 Talence, France

[3] LIMMS/CNRS-IIS (UMI2820), Institute of Industrial Science, The University of Tokyo, 4-6-1 Komaba, Meguro-ku, Tokyo, 153-8505, Japan

[4] CSIRO Energy Centre, Mayfield West, NSW 2304, Australia

[5] Advanced Light Source, Lawrence Berkeley National Laboratory, Berkeley, CA 94720, USA

[6] School of Aerospace, Mechanical and Mechatronic Engineering, The University of Sydney, Camperdown, NSW 2006, Australia

*Corresponding Author: Natalie P. Holmes, natalie.holmes@newcastle.edu.au

Keywords

Eco-friendly processing, waterborne colloids, non-fullerene acceptor, morphology, nanoengineering, X-ray spectromicroscopy, surface energy, printed electronics

Abstract

The emerging field of printed electronics requires environmentally friendly solution-processable electroactive materials. This can be achieved by the development of waterborne colloidal dispersions. Functionality in these composite materials can be tuned by thermodynamically modifying the material morphology, often by creation of kinetically stabilized aqueous nanoparticle dispersions. In this work we demonstrate that the internal structure of organic nanoparticles is controlled by the surface energy difference between the polymeric donor material and the non-fullerene acceptor (NFA) material. Nanoparticles of the following donor-acceptor combinations, suitable for printed organic photovoltaics, have been synthesized: TQ1:N2200, TQ1:PNDIT10, P3HT:N2200, P3HT:o-IDTBR and P3HT:eh-IDTBR . Advanced synchrotron-based X-ray spectroscopy and microscopy are used to correlate the formation of core-shell nanoparticle morphology to the material surface energy. We subsequently present a viable avenue for customizing the blended nanoparticle structure into (i) core-shell, (ii) molecularly intermixed, or (iii) inverted shell-core structures. Our results showed that TQ1:PNDIT10 and P3HT:o-IDTBR nanoparticles were comprised of a donor-rich shell and an NFA-rich core, however, interestingly

we show a reversal to the inverse NFA shell / donor core structure for TQ1:N2200, P3HT:N2200 and P3HT:eh-IDTBR nanoparticles, driven by the low surface energy of N2200 (23.7 mJ m^{-2}) and eh-IDTBR (18.3 mJ m^{-2}). This article is the first report of a flipped nanoparticle core-shell morphology comprising an NFA-rich shell for the miniemulsion synthesis route. The composition of the shells and cores was able to be controlled by the differential mismatch in the surface energy of the donor and acceptor materials, with $\triangle G_{surface} > 0$, $\triangle G_{surface} = 0$, and $\triangle G_{surface} < 0$ for acceptor core - donor shell, molecularly intermixed, and acceptor shell - donor core, respectively. Accordingly, this introduces an entirely overlooked new figure of merit (FoM) for customizing nanoparticulate colloidal inks: tunable *surface energy* of non-fullerene-based semiconductors. The establishment of this FoM opens up electroactive material design to a wide range of functional printing applications with varying device and ink structure requirements, thereby reshaping the nanoengineering toolkit for waterborne colloidal dispersions and hence printed electronics.

Introduction

Nanoparticles formed from electroactive materials have been heavily studied as the fundamental building blocks within numerous multidisciplinary fields. Such interest arises from a well-established ability to obtain differences in chemical, electrical, optical, and structural properties in nanostructured materials compared to their bulk analogues. The ability to tune these nanomaterial properties through relatively simple synthetic chemical modifications that control nanoparticle size, shape, and function has allowed ground-breaking advances in catalysis,[1–5] quantum dots,[6–8] biosensors and medical diagnostics,[9–12] transistors,[13] photovoltaics,[14,15] and printed electronics.[16–18] Successful incorporation of desirable nanoscale structure requires control of the interactions of individual materials with their surroundings, including other reagents such as secondary electroactive materials, solvent molecules, additives and stabilizing surfactant interfaces.[19,20]

In recent years, technology based on solution-processable electroactive organic molecules for organic photovoltaics (OPV) has made a big step forward due to the rapid development of non-fullerene acceptors (NFAs). This new class of organic semiconductors offers several advantages compared to the commonly used fullerene derivatives as the NFA chemical structure can be tuned through synthetic chemistry routes to modify optoelectronic properties. Advantages delivered through this synthetic flexibility include broad and strong optical absorption, bandgap (E_g) tunability, reduced synthetic costs and superior morphological stability in device applications.[21,22] These new materials are already producing exceptional results in printed electronics, including OPV, demonstrating record power conversion

efficiencies (PCE) that exceed 18%.[23,24] However, although organic printable technology has many reported advantages,[25] the technology is not yet eco-friendly. One of the remaining challenges is the replacement of the halogenated and/or aromatic solvents (such as chloroform, dichloromethane and chlorobenzene) with environmentally friendly inks. The most attractive alternative in this regard is to move to water-based inks. The first efforts to shift from organic solvents to water appeared in 2002 with the work of Landfester et al.[26–28] The authors applied a miniemulsion method to create blended donor and acceptor nanoparticles. Despite a poor device performance in comparison to blended bulk solutions – the concept of waterborne nanoparticulate organic electroactive inks was born. For some years, polymer donor and fullerene acceptor materials were employed exclusively, with various thermodynamic treatments investigated to try and tune the nanoparticle structure. However, the electronic devices fabricated from these nanoparticle inks always exhibited poorer performance than their bulk solution counterparts.[29] More recently, P3HT was replaced by a low band-gap polymer, PBDTTPD,[30] which in combination with fullerene derivatives was able to increase device performances observed in photovoltaic devices (PCEs up to 3.8%), however, performance still remained about half of that observed for the bulk solution mixtures. In 2018, Xie et al.[15] combined the nanoprecipitation method, an alternative method to generate nanoparticles dispersed in water,[31] and the use of a surfactant (poloxamer Pluronic F127) to synthesize a different kind of donor:NFA nanoparticle. Using a surfactant-stripping technique, they managed to remove the excess of surfactant and obtained a step-change advance in device performance (PCE of 7.5% with PBQ-QF:ITIC). Critically, key performance metrics in devices created from a blended nanoparticle ink now approached that obtained for the intermixed bulk solution.[15] This last report indicates that developing waterborne nanoparticulate electroactive inks with NFAs is a promising route towards high performance eco-friendly printed electronic devices. Nonetheless, there remains a lack of understanding regarding the specifics of deliberately engineering performance in these nanoparticle ink systems. Indeed, over the past decade, the switch to new donor and acceptor materials has improved device performance in conjunction with improved optoelectronic properties of the materials (such as enhanced light absorption or band energy modulations). However, it was not until the most recent reports of NFA investigations where the nanoparticle device performance suddenly began to rival that of the bulk solution counterparts.[15] This development suggests that there is an additional benefit to the NFA materials that has not been available in the past; the ability to tune the nanoscale morphology in addition to the optoelectronic properties of the nanoparticles.

Fullerene derivatives have been for many years the standard organic semiconductor used as solution-processable electron acceptors in printed electronics applications.[32,33] When employed in combination

with a polymeric donor, the resulting morphology in the nanoparticle synthesized via miniemulsion is almost always reported to form a core-shell structure with a fullerene-rich core.[29,34–38] This nanostructure has been attributed to the higher surface energy of fullerene derivatives ($PC_{61}BM$ - 38.2 mJ m^{-2} and $PC_{71}BM$ - 39 mJ m^{-2}) compared to polymeric donors, but has been shown to be problematic for achieving high device performances.[39] Variations in the donor polymer materials have been unsuccessful in altering this non-optimal morphology, as the surface energies cannot approach those of the extremely high values characteristic of nanospherical fullerene materials. Indeed, these low surface energies could be considered as a roadblock for the rational design of organic blended nanoparticles. Some reports provide evidence for the nature of the surfactant playing a role in the resulting morphology of organic nanoparticles. In particular, using sodium 2-(3-thienyl)ethyloxybutylsulfonate (TEBS) instead of sodium dodecyl sulfate (SDS), Subianto et al.[40] and Kosco et al.[41] reported that a core-shell morphology for P3HT:$PC_{61}BM$ nanoparticles and PTB7-Th:eh-IDTBR nanoparticles, respectively, was changed to a mixture of donor-rich and acceptor-rich interspersed nano-domains. This change was attributed to the similarity in chemical structure of the TEBS surfactant to both donor and acceptor material, and also chloroform/water interfacial tensions which are equal when the chloroform phase contains the donor or the acceptor leading to the migration of both donor and acceptors at the water/chloroform interface (shell). Although playing with the interfacial tension is a good strategy to attain the desired initial particle morphology, overall it might not be thermodynamically favorable as the surface energy mismatch of the donor and acceptor components would lead to, upon thermal treatment of a nanoparticle film in a device, larger phase separation.

With the emergence of NFAs, the available synthetic chemistry routes to modify the molecular structure, and as a consequence the surface energy, is far greater than for fullerene derivatives. Thus, these NFAs form an ideal set of molecules to investigate how modifications to the surface chemistry of the acceptors can change nanoparticle formation thermodynamics; and consequently the charge carrier kinetics and electronic functionality of blended nanoparticle inks. With this wide range of acceptor materials, it is possible to investigate how to combine the established green ink processability of aqueous nanoparticles[42] with the ability to engineer truly customized nanostructures.[43] Such nanoengineered NFA blends offer an attractive option for the field of printed electronics and developing new fundamental physical chemistry insights into nanoscale structure-property relationships.

In this work, we provide the first in-depth study of the self-organization of various kinds of composite organic semiconductor nanoparticles as a function of their surface energy (the interfacial free energy of

a surface). Two polymeric donors (TQ1 and P3HT) were combined with different types of molecular and polymeric NFAs (PNDIT10, N2200, o-IDTBR, eh-IDTBR), and a wide range of techniques were used to elucidate the nanostructure of the resultant nanoparticles: transmission electron microscopy (TEM), scanning electron microscopy (SEM), near edge X-ray absorption fine structure (NEXAFS) spectroscopy and scanning transmission X-ray microscopy (STXM). The external shape obtained for all particles was found to be mainly driven by the semi-crystalline properties of the donor polymer. Nanoparticles including P3HT present a wrinkled texture while those prepared with amorphous TQ1 present a smoother texture. The internal composition of the nanoparticles was elucidated by STXM – the analysis of the different STXM compositional maps shows that the outer region of the particle (shell) is predominantly composed of the lowest surface energy materials. Indeed, through the tunability of the NFA surface energies across a wide range (18.3 to 30.1 mJ m^{-2}), we are able to demonstrate for the first time that the internal nanoscale structure of the nanoparticles is directly correlated to the surface energy differential between the blend materials for a comprehensive set of material systems. This general trend of the self-organization defines a critical new design rule for directing the morphology of organic semiconductor nanoparticles into desired structures. The ability to control the functionality of organic nanoparticle inks through chemical synthesis pathways to tuning the nanoparticle structure provides an invaluable new tool across a wide range of research applications.

Experimental

Materials

Poly{[N,N'-bis(2-octyldodecyl)naphthalene-1,4,5,8-bis(dicarboximide)-2,6-diyl]-alt-5,5'-(2,2'-bithiophene)} (N2200) (also named PNDI(2OD)2T) was purchased from Ossila (M_n 150,500 Da, size dispersity (Đ) 1.93). Poly{{[N,N'-bis(2-octyldodecyl)naphthalene-1,4,5,8-bis(dicarboximide)-2,6-diyl]-alt-5,5'-(2,2'-bithiophene)}-ran-{[N,N'-bis(2-octyldodecyl)naphthalene-1,4,5,8-bis(dicarboximide)-2,6-diyl]-alt-2,5-thiophene}} (PNDIT10) was purchased from Ossila (M_n 78,960 Da and Đ 2.40). o-IDTBR and eh-IDTBR were purchased from 1-Materials. TQ1 (M_n 53,100 Da, Đ 2.5) was synthesized by the copolymerization of monomers 5,8-dibromo-6,7-difluoro-2,3-bis(3-(octyloxy)phenyl) quinoxaline and 2,5-bis(trimethylstannanyl)thiophene, with the procedure described in detail elsewhere.[34,44] Poly(3-hexyl thiophene) (P3HT) was synthesized as described by Holmes et al.[35] The chemical structures of the two polymer donor materials and four NFA materials are provided in Figure 2b. Sodium dodecyl sulfate (SDS) surfactant and chloroform solvent were purchased from Sigma-Aldrich.

The surface energy of PNDIT10 was measured via optical tensiometry. Thin films of PNDIT10 were prepared on freshly cleaned and plasma treated microscope slides (10 mg/mL solution in chloroform, 3000 rpm, 30 s, no annealing). The measurements were performed on a Biolin Scientific Attension Theta Optical Tensiometer. 2 µL of liquid was manually deposited onto the film with a gas chromatography syringe, and video footage recoded at 12 frames per second for the duration of the measurement. Contact angles were fitted with the Young-Laplace expression. Diiodoethane (CI_2H_2, 99% stored over Cu stabilizer, Sigma-Aldrich) and freshly prepared milli-Q H_2O (resistivity >18.3 MΩ cm) were used for contact angle measurements on the polymer films. The tensiometer was calibrated with a 4000 ± 1.0 µm standard tungsten carbide precision calibration ball. Measurements were performed at 22 °C at 30 % RH and ran in triplicate.

Nanoparticle Synthesis

To generate the waterborne nanoparticle inks, organic solvent is used in the miniemulsion oil phase, but importantly, only a small volume is used, and this small volume of solvent is removed via evaporation such that later use of the inks in applications such as solar cell printing, do not involve organic solvents. The miniemulsion organic phase ("oil" phase) was prepared by dissolving 15 mg of donor material (P3HT or TQ1) and 15 mg of acceptor material (PNDIT10 or N2200) for 1:1 donor:acceptor systems, or 20 mg of donor material and 10 mg of acceptor material for 2:1 donor:acceptor systems, in 1.08 mL chloroform. In future large-scale nanoparticle synthesis, the chloroform can be substituted for a non-chlorinated oil phase solvent such as toluene or xylene. Also, the organic solvent can be reused in a closed synthesis cycle. The volume of organic solvent was increased to 1.62 mL for the donor:acceptor systems incorporating N2200, due to the large molecular weight of N2200 and the associated high viscosity solution. The miniemulsion aqueous phase was prepared by dissolving 0.5 mg of SDS surfactant in 2.8 mL of Milli-Q® filtered water. The surfactant concentration was purposely low so as to achieve a broad distribution in nanoparticle sizes for STXM imaging. Macroemulsions were generated by combining the organic and aqueous phases and stirring at 1100 rpm, 33 °C for 1 h. A miniemulsion was generated using ultrasonication via a Hielscher UP400S ultrasonic processor with a 7 mm diameter tip. Sonication was at 30 W for 2 min, with an amplitude setting of 50%, an ice bath was used to prevent overheating of the sample. Following sonication, the miniemulsion was transferred immediately to a hot plate for organic solvent evaporation at 60 °C with rapid stirring. This evaporation was performed for a minimum of 3 h to ensure complete removal of organic solvent. The total volume of the nanoparticle inks was reduced to 0.5 mL via centrifugal dialysis. P3HT:eh-IDTBR nanoparticles were also

synthesized via the nanoprecipitation method. A tetrahydrofuran (THF) solution of P3HT:eh-IDTBR was prepared at a total concentration of 5 mg/mL and a donor:acceptor ratio of 1:1. The THF solution was stirred at 60 °C for 2 h and then kept at 55 °C. For the non-solvent phase, 4.5 mL of deionized water was added to a 6 mL vial and heated at 55 °C under moderate stirring (300 rpm). 0.5 mL of THF solution was inserted quickly into the water containing vial. The dispersion was removed from the hot plate and cooled down at room temperature for 10 min, then subsequently filtered with a 5 μm filter. An additional evaporation step was applied, to evaporate the THF the dispersion was left stirring at 300 rpm on a hot plate at 60 °C for 3 h with the lid open.

NEXAFS Spectroscopy

NEXAFS measurements of TQ1, P3HT, N2200, PNDIT10 and o-IDTBR were performed on beamline 5.3.2.2 at the Advanced Light Source (ALS) synchrotron in Berkeley, California. Pristine films of TQ1, P3HT, N2200, PNDIT10, o-IDTBR and eh-IDTBR were prepared by spin coating chloroform solutions of each semiconductor material onto PEDOT:PSS (Clevios P VP AI 4083, purchased from H.C. Starck) coated glass substrates. 2 × 2 mm^2 sections were scored on the films using a scalpel, followed by floating off the film sections onto a D.I. water surface, which was made possible by dissolving the PEDOT:PSS sacrificial layer under the semiconductor material films. 2 × 2 mm^2 film sections were subsequently collected onto 300 mesh Cu grids (20 μm bar, 63 μm hole, 3 mm diameter, purchased from ProSciTech Pty Ltd) for NEXAFS measurements. The energy of the X-ray beam was varied between 270 and 340 eV, spanning the C K-edge region with an energy resolution of 0.1 eV. Second- and third- order light was removed by an order sorting aperture and also N_2 gas filter (further details are provided in Kilcoyne *et al*.[45]). Energy calibration at the C K-edge was performed using CO_2 gas (peak at 292.74 eV).

NEXAFS measurements of eh-IDTBR were performed on the PolLux beamline (X07DA) at the Swiss Light Source (SLS) synchrotron, with similar measurement parameters to those used at the ALS. The energy of the X-ray beam was varied between 270 and 340 eV, spanning the C K-edge region with an energy resolution of 0.15 eV. Dwell times were increased to 10 and 12 ms to account for lower flux at SLS PolLux compared to ALS 5.3.2.2.

Orthogonal energies were determined from NEXAFS spectra of pristine films of P3HT, TQ1, PNDIT10, N2200, o-IDTBR and eh-IDTBR.

X-ray Spectromicroscopy

STXM measurements were performed on beamline 5.3.2.2 at the ALS synchrotron. Samples were prepared for STXM measurements by spin coating 2.5 μL of nanoparticle ink onto low stress silicon nitride (Si_3N_4) membrane windows with silicon dioxide coating (window dimensions 0.25 × 0.25 mm^2, window thickness 15 nm, silicon frame dimensions 5 × 5 mm^2, purchased from Norcada, Canada) at 3000 rpm, 1 min, low acceleration of 112 rpm/s. Samples were air dried at room temperature. The samples on Si_3N_4 windows were loaded in the STXM sample chamber and rastered with respect to the X-ray beam. The STXM sample chamber was backfilled with helium (0.33 atm). The transmitted X-ray beam is detected by a scintillator and a photomultiplier tube. The STXM Fresnel zone plate had an outer most zone width of 25 nm, setting the spatial resolution limit of the measurement. Singular value decomposition (SVD) was used to fit a sum of the pristine material NEXAFS spectra to the measured blend spectrum of the nanoparticles – at each pixel – in the STXM images. Prior to SVD fitting, the pristine material NEXAFS spectra are normalized to film thickness. The method of reference-spectrum normalization constitutes dividing the real spectrum by a theoretical spectrum calculated based on the material's chemical formula using henke.lbl.gov/optical_constants/filter.html. The aXis2000 package was used to perform image analysis of STXM maps.

Electron Microscopy

TEM was used to reimage the same nanoparticles, where possible, for collecting position-matched micrographs. The Si_3N_4 substrates with deposited nanoparticles were transported back to the University of Newcastle (Australia) to measure TEM on a JEOL 1200 EXII at an accelerating voltage of 80 kV at varying magnification ranges.

Samples were prepared for SEM by spin coating 2.5 μL of the nanoparticle inks (3000 rpm, 1 min, low acceleration of 112 rpm/s) onto highly doped silicon substrates (Type P (boron), <111>, resistance of 1–30 Ω, roughness of 2 nm, purchased from ProSciTech Pty Ltd). The silicon substrates were first UV-ozone cleaned for 10 min. SEM was performed on a Zeiss Sigma VP FESEM operating at an accelerating voltage of 2 kV.

Results and Discussion

Materials Selection and Surface Energy

Two polymeric donors (TQ1 and P3HT), two polymeric NFAs (N2200, PNDIT10) and two small molecule NFAs (o- and eh- IDTBR) were chosen for this study. We took advantage of the new range of

low bandgap NFAs with desirable properties such as tunable bandgap and broad light absorption. N2200 is a naphthalene diimide (NDI) based polymer, which provides high electron affinity, electron mobility, strong absorption in the visible and near-infrared region and good solubility.[22] Critically, the imide functionality also produces a relatively low surface energy. PNDIT10 is a structural analogue of N2200 generated by replacing a number of bithiophene (2T) units in the N2200 backbone by single thiophene (T) units, where T10 represents the percentage of the single T at 10%.[22] PNDIT10 has a more flexible backbone and lower crystallinity than N2200 due to its reduced regularity in the main chain, which also modulates the surface energies to higher values.[22] IDTBR derivatives have been employed in this study as additional NFAs with variable surface energies. IDTBR acceptors were developed by Holliday et al. in 2016,[21] and consist of side-chain engineering from a common core, with a linear (n-octyl) alkyl chain generating the molecule o-IDTBR, yielding a higher surface energy crystalline material, while the branched 2-ethylhexyl side-chain structural analogue (eh-IDTBR) has a lower surface energy and is mostly amorphous.[21]

The key material properties utilized to select an acceptor material for OPV fabrication, namely HOMO, LUMO, E_g, λ_{max}, are listed in Table 1, with the UV-Vis absorbance spectra provided in Figure S1 (Supplementary Material). The selection of materials for this study was aimed at understanding the influence of physico-chemical properties, such as surface energy, on the donor-acceptor nanoparticle morphology, hence the surface energy of the acceptor ranges from 18.3 to 30.1 mJ m^{-2} (Table 1). Conveniently, the similarity of the structural analogs selected (N2200 and PNDIT10; o-IDTBR and eh-IDTBR) also enabled an investigation of the impact of material crystallinity on the self-assembly of the nanoparticles. With the exception of the NFA polymer PNDIT10, the surface energy of the polymers and small molecules used in nanoparticle synthesis are found in the literature.[46–51] We characterized the surface energy of PNDIT10 using Fowkes' Theory[52] and the two-drop method to be 30.1 mJ m^{-2}, largely dominated by the dispersive contribution (see Table 1 and Supplementary Material).

Table 1. Surface energy, HOMO, LUMO, optical bandgap (E_g) and λ_{max} of donor and acceptor materials.

Material	HOMO / LUMO (eV)	E_g (eV)	λ_{max} (nm)	Surface Energy (mJ m^{-2})
Donor				
TQ1	-5.7 / -3.3 [44]	1.7 [44]	362, 622 [a]	29 [46]
P3HT	-5.2 / -3.2 [53]	1.9 [54]	522 [a]	26.9 [47]
Non-fullerene acceptor				
PNDIT10	-6.36 / -4.05 [22]	1.55 [22]	344, 600 [a]	30.1
N2200	-6.26 / -4.06 [22]	1.44 [22]	393, 703 [a]	23.7 [48,49]
o-IDTBR	-5.51 / -3.88 [21]	1.63 [21]	690 [a]	28.1 [50]

eh-IDTBR	-5.58 / 3.90 [21]	1.68 [21]	672 [a]	18.3 [51]
Fullerene acceptor (for comparison purposes)				
$PC_{61}BM$	-5.80 / -3.80 [55]	2.0 [b]	350 [56]	38.2 [57]
$PC_{71}BM$	-5.9 / -3.7 [58]	2.2 [b]	475 [34]	39 [46]

[a] Supplementary Material

[b] Electronic bandgap (determined from UPS/IPES), whereas for all other materials the optical bandgap is listed.

Nanoparticle Synthesis and Electron Microscopy

Two component nanoparticles were synthesized via the miniemulsion method for the donor-acceptor material systems TQ1:N2200, TQ1:PNDIT10, P3HT:N2200, P3HT:o-IDTBR and P3HT:eh-IDTBR. A 1:1 w/w ratio was applied to all systems, with the exception of the TQ1:N2200 system where both a 1:1 and a 2:1 w/w ratio were studied. For the P3HT:eh-IDTBR system, nanoparticles were also synthesized via the nanoprecipitation method, and both miniemulsion nanoparticles and nanoprecipitation nanoparticles were analyzed with STXM, Figure S5 and Figure 4k-n, respectively.

Prior to investigation of the nanoparticle substructure for each system with synchrotron-based X-ray microscopy, SEM measurements of the nanoparticle samples were performed to assess the (1) shape and surface texture of the particles, (2) particle size and size distribution, and the (3) particle packing and film formation (Figure 1). P3HT:N2200 nanoparticles are angular, non-spherical in shape and possess a wrinkled surface texture (Figure 1d); attributed to the crystallinity of both P3HT and N2200 polymers.[22,32] The presence of crystalline P3HT domains in the P3HT:N2200 nanoparticles is further confirmed by the vibronic peaks[59,60] at 560 and 610 nm in the UV-Vis absorbance spectrum of the nanoparticle ink (Figure S2). TQ1:PNDIT10 and TQ1:N2200 nanoparticles (both 1:1 and 2:1) are predominantly spherical in shape and smooth in texture (Figure 1a-c); TQ1 is an amorphous polymer combined with the semi-crystalline polymer N2200.[61] PNDIT10 is also a semi-crystalline polymer, but less crystalline than N2200.[22] The P3HT:o-IDTBR and P3HT:eh-IDTBR nanoparticles are predominantly spherical in shape and wrinkled in texture (Figure 1e-f). o-IDTBR is a more crystalline material than eh-IDTBR,[21] combined with the crystalline polymer P3HT likely contributing to the wrinkled surface texture of the nanoparticles.

The particle size and size distribution for each nanoparticle sample is tabulated in Table 2, with the mean value used as an indicator of nanoparticle size and the standard deviation (σ) used as an indicator of the size distribution. The nanoparticle size was measured by applying a circular Hough transform algorithm to SEM images of nanoparticle films, according to our previously reported method.[34] This method gave diameters of 233 ± 105 nm for the TQ1:PNDIT10 nanoparticles; 172 ± 74 nm for the 1:1 TQ1:N2200 nanoparticles; and 139 ± 50 nm for the 2:1 TQ1:N2200 nanoparticles. For the nanoparticles synthesized

with P3HT donor material, the Hough transform analysis gave diameters of 212 ± 81 nm for the P3HT:o-IDTBR nanoparticles and 170 ± 89 nm for the P3HT:eh-IDTBR nanoparticles. The P3HT:N2200 nanoparticle diameter of 233 ± 132 nm listed in Table 2 represents the particle length, as these nanoparticles were not spherical and hence the circular Hough transform MATLAB code was not suitable. The particle sizes reported in Table 2 have been customized to optimize STXM imaging.

The particle packing and film formation can be easily visualized in the SEM in Figure 1. Regions of randomly close packed (RCP)[62,63] arrays are evident in all six film types. Regions of hexagonally close packed (HCP)[64] arrays are more common in samples which are more monodisperse, that is, have a narrow size distribution and predominantly spherical particles. There is evidence of HCP arrays in the TQ1:PNDIT10, 1:1 TQ1:N2200, 2:1 TQ1:N2200 and P3HT:o-IDTBR nanoparticle samples (Figure 1a,b,c and e).

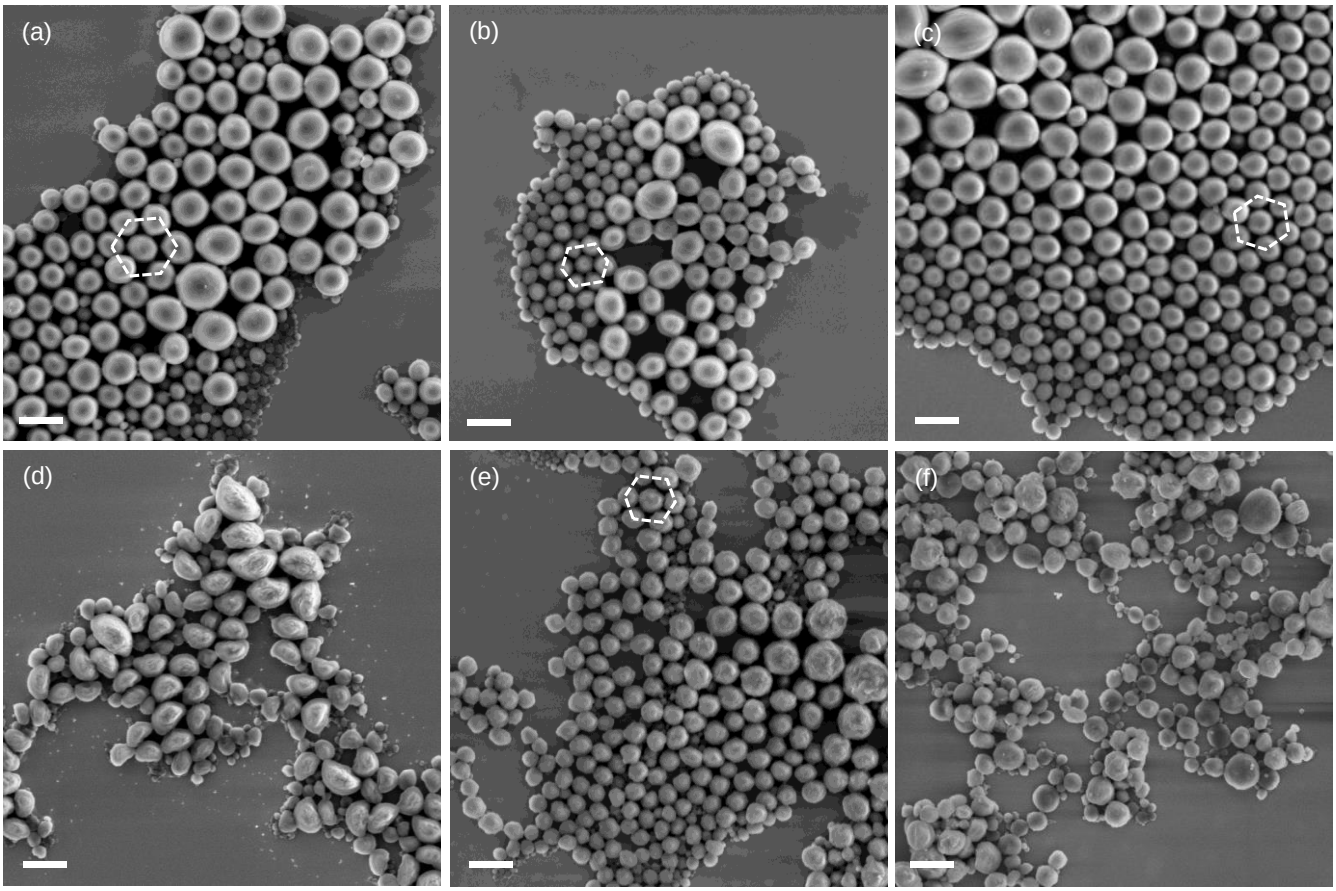

Figure 1. SEM of (a) 1:1 TQ1:PNDIT10 nanoparticles, (b) 1:1 TQ1:N2200 nanoparticles, (c) 2:1 TQ1:N2200 nanoparticles, (d) 1:1 P3HT:N2200 nanoparticles, (e) 1:1 P3HT:o-IDTBR nanoparticles, and (f) 1:1 P3HT:eh-IDTBR nanoparticles. Scale bar is 500 nm. Examples of HCP are identified in (a), (b), (c) and (e).

Table 2. Nanoparticle properties: Shape and surface texture; nanoparticle size calculated using circular Hough transform analysis of SEM images (>1200 nanoparticles sampled for each material system); nanoparticle film packing classification.

Donor-Acceptor System	Shape / Surface Texture	Nanoparticle Diameter (Mean ± σ) (nm)	Packing Classification
NFAs combined with TQ1 donor			
1:1 TQ1:PNDIT10	Predominantly spherical / Smooth	233 ± 105	HCP, RCP
1:1 TQ1:N2200	Predominantly spherical[d] / Smooth	172 ± 74	HCP, RCP
2:1 TQ1:N2200	Predominantly spherical[d] / Smooth	139 ± 50	HCP, RCP
NFAs combined with P3HT donor			
1:1 P3HT:N2200	Angular & non-spherical / Wrinkled	233 ± 132 [c]	RCP
1:1 P3HT:o-IDTBR	Predominantly spherical / Wrinkled	212 ± 81	HCP, RCP
1:1 P3HT:eh-IDTBR	Predominantly spherical / Wrinkled	170 ± 89	RCP

[c] The P3HT:N2200 nanoparticles were not spherical, hence the diameter value represents the particle length.
[d] Some instances of prolate spheroids.

NEXAFS Spectroscopy of NFAs, Orthogonal Energy Identification for STXM

NEXAFS spectra were collected in transmission mode at the ALS synchrotron on beamline 5.3.2.2, and at the SLS synchrotron on the PolLux beamline (X07DA) for material eh-IDTBR. Figure 2 presents the NEXAFS spectra of donor polymers TQ1 and P3HT, and the NFA materials N2200, PNDIT10, o-IDTBR and eh-IDTBR.

STXM (a spatially-resolved variant of transmission NEXAFS spectroscopy)[45] was utilized as a high-resolution imaging technique with chemical sensitivity to collect X-ray maps of nanoparticle films at multiple photon energies of the incident beam. A careful selection of the photon energy for each X-ray map was performed, establishing the orthogonal energies, and singular value decomposition (SVD) employed to determine the relative ratio of components (at each pixel) for a blend film.[65] Orthogonal energies were chosen prior to collecting X-ray maps by directly comparing the NEXAFS spectra of pristine films of each of the blend film components and finding specific energies with a marked difference in X-ray absorption for each of the component materials. A not inconsiderable challenge presented by moving to NFAs[66] is the increased difficulty in analyzing STXM stack data produced from these polymer-donor:NFA blend films. The difficulties are twofold: firstly NFAs typically possess far fewer sp^2-bonding environments, leading to a diminished (or non-existent) C1s-pi* transition peak.[15] Secondly,

these NFAs are often polymers, which offer up relatively similar chemistry to the polymer materials used as donor materials. As such, the NEXAFS spectra of the components of the polymer-donor: NFA blend film tend to be much more similar than is typically the case for the more traditional systems incorporating fullerene-acceptors.

For a representative polymer-donor:NFA system – namely a 1:1 blend of P3HT and o-IDTBR – four different energies (284.1, 285.4, 287.7 and 291.0 eV) were trialed as the orthogonal set (Figure S4). Of these energies, only 285.4 eV could be considered an obvious candidate, utilizing a large difference in absolute absorption between the two components. 284.1 eV constitutes an energy typically categorized as pre-carbon K-edge (for amorphous carbon materials), and offers up a situation whereby one component of the blend film has commenced absorbing at said K-edge, whilst the other component has not (to within the background absorption level). The disadvantage of using such a "pre-edge" energy is that the absolute absorption of even the "absorbing" component is very small, which can potentially lead to a lot of noise in the final stack analysis. On the other hand, whilst 291.0 eV does not appear as an obvious energy choice for component analysis, the very high absolute absorption at these higher "post-edge" energies lends itself to a relatively enhanced difference in signal for the two components. Although, note that if the difference in absorption for the two components at this energy is very small, this can also lead to more noise appearing in the final analysis, much as in the case for the pre-edge energy. The orthogonal energies selected for STXM analysis are listed in Table S1, and further detail of optimizing measurement conditions for these polymer-donor:NFA systems is provided in Supplementary Material.

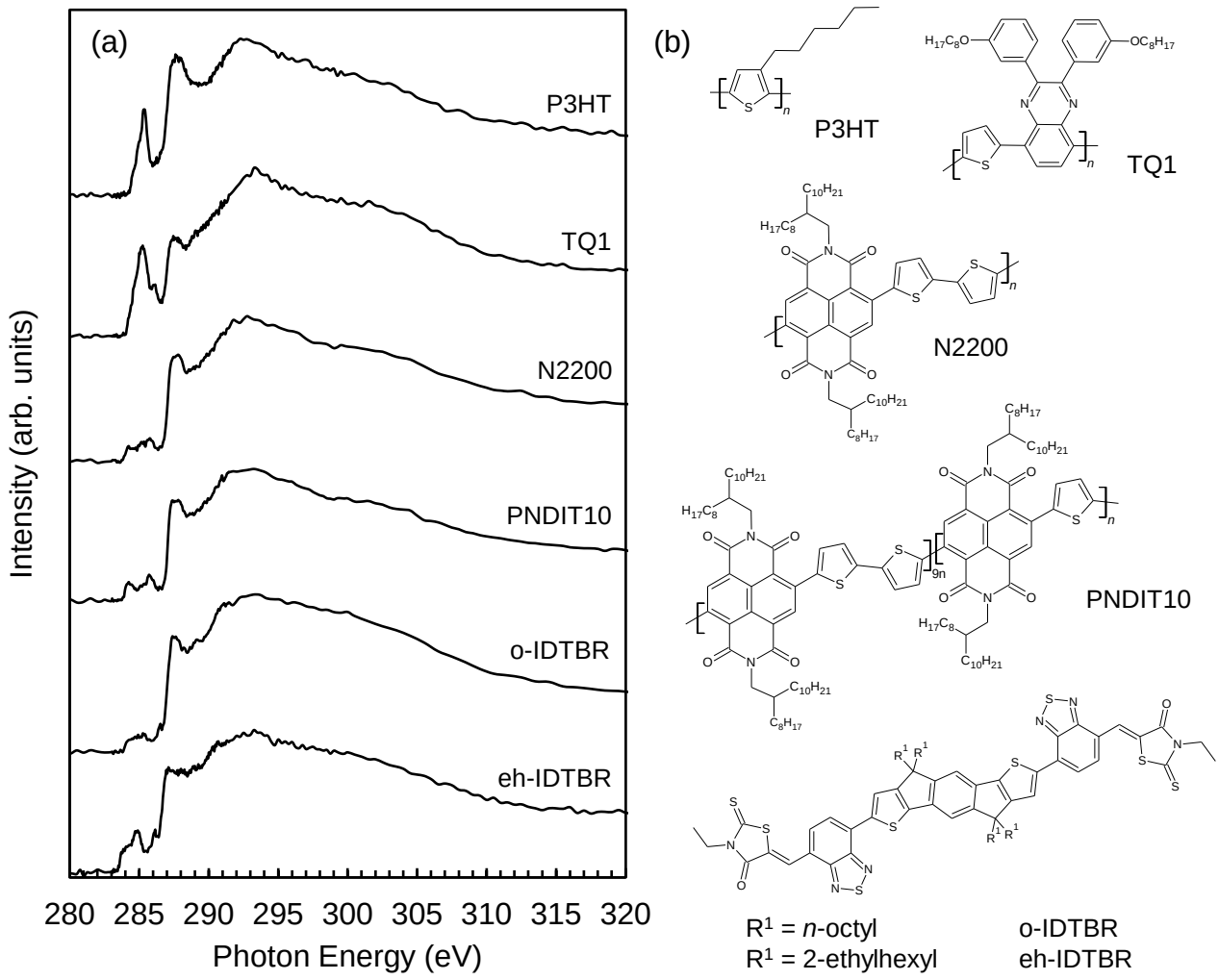

Figure 2. (a) NEXAFS spectra and (b) chemical structures of donor materials P3HT and TQ1; and non-fullerene acceptor materials N2200, PNDIT10, o-IDTBR and eh-IDTBR.

Nanoparticle Structure via Self-Assembly

STXM measurements were carried out using beamline 5.3.2.2 at the ALS synchrotron to ascertain the internal nanostructure of the donor-acceptor nanoparticles. STXM composition maps were collected, together with position-matched TEM, for 1:1 TQ1:PNDIT10, 1:1 TQ1:N2200, 2:1 TQ1:N2200 (Figure 3) and 1:1 P3HT:N2200, 1:1 P3HT:o-IDTBR, 1:1 P3HT:eh-IDTBR (Figure 4) nanoparticles. As will be discussed in detail shortly, a core-shell structure was measured for all donor-acceptor systems studied, and so the STXM compositional maps were utilized to calculate the donor and acceptor material concentrations in the nanoparticle shell and core domains. STXM is a transmission technique, hence the nanoparticle core compositions were calculated by subtracting the nanoparticle shell contribution from

the composition at the nanoparticle centre (with the full method reported elsewhere in the literarure[35]). A typical radial profile of a nanoparticle synthesized for each material system is plotted in Figure 5 (with detail on the method for deriving radial profiles provided in Supplementary Material), and the composition of the nanoparticle core and shell domains for each material system studied is listed in Table 3.

A core-shell structure was measured for all six nanoparticle types studied with STXM, with the shell and core composition varying depending on the donor-acceptor material combination. The core-shell structure was derived from the STXM maps (Figure 3 and Figure 4) for each system by extracting the radial profiles of the nanoparticles (Figure 5), which show an increase of one component from particle centre to particle perimeter. For example, for TQ1:PNDIT10 nanoparticles, the TQ1 composition is low at the particle centre in Figure 5a, but the TQ1 concentration increases to >75% at the particle perimeter. This composition difference is also visibly evident in the STXM maps themselves, where a bright "ring" appears around the particles in Figure 3a for example, reflecting a high concentration of TQ1.

For the TQ1:NFA nanoparticle systems characterized via STXM, a TQ1-rich shell (80 ± 4%) and PNDIT10-rich core (84 ± 9%) was measured for the TQ1:PNDIT10 nanoparticles, as depicted in Figure 3a-e. For the TQ1:N2200 nanoparticles, the structure inverted to a TQ1-rich core for both 1:1 (Figure 3f-j) and 2:1 (Figure 3k-o) donor:acceptor ratios. An N2200-rich shell is evident by the bright rings observed in the N2200 STXM fractional composition map for the 1:1 (Figure 3g) and the 2:1 (Figure 3l) TQ1:N2200 nanoparticles. The composition was measured as 55 ± 3% and 53 ± 5% for the N2200-rich shells for the 1:1 and 2:1 TQ1:NN2200 nanoparticles, respectively, and the composition of the TQ1-rich cores was 92 ± 5% and 87 ± 9% for the 1:1 and 2:1 TQ1:N2200 nanoparticles, respectively.

Looking now at the P3HT:NFA nanoparticles characterized using STXM (as shown in Figure 4), the location of the P3HT in the nanoparticles flipped from core to shell – then back to core – as the NFA was changed from N2200 to o-IDTBR to eh-IDTBR. An N2200-rich shell (61 ± 7%) and P3HT-rich core (91 ± 6%) was measured for the P3HT:N2200 nanoparticles, as depicted in Figure 4a-e. For the P3HT:o-IDTBR nanoparticles, a P3HT-rich shell (69 ± 6%) and o-IDTBR-rich core (74 ± 16%) was measured (Figure 4f-j). For the IDTBR nanoparticle series, the IDTBR core inverts to an IDTBR-rich shell for the P3HT:eh-IDTBR nanoparticles synthesized via both nanoprecipitation (Figure 4k-o) and miniemulsion (Figure S5). A composition of 71 ± 6% is measured for the eh-IDTBR-rich shells and a composition of 61 ± 7% is measured for the P3HT-rich cores.

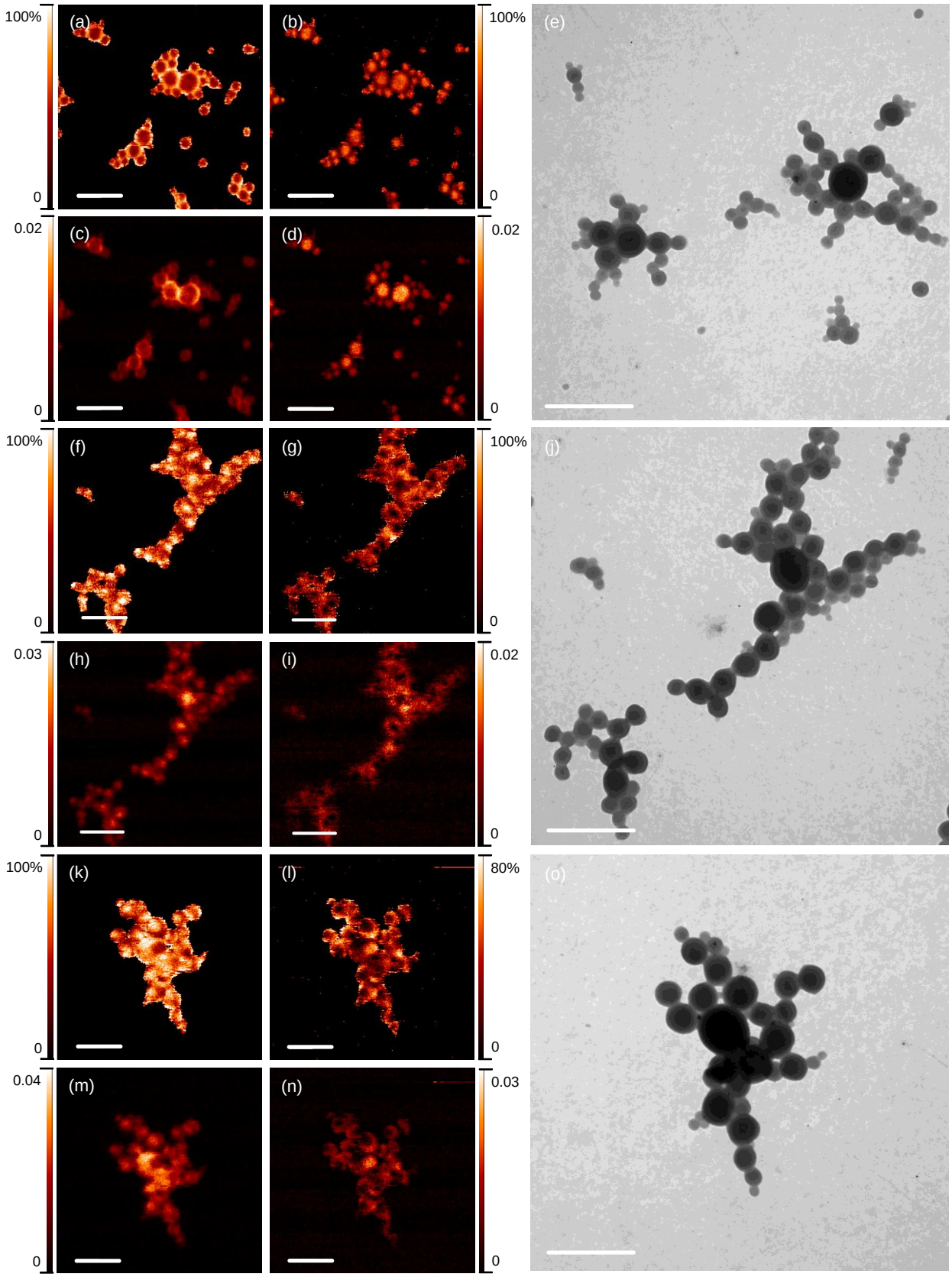

Figure 3. STXM fractional composition maps showing the concentration of (a) TQ1 and (b) PNDIT10 with corresponding STXM mass plots (c and d) and (e) TEM for 1:1 TQ1:PNDIT10 nanoparticles; STXM fractional

composition maps showing the concentration of (f) TQ1 and (g) N2200 with corresponding STXM mass plots (h and i) and (j) position-matched TEM for 1:1 TQ1:N2200 nanoparticles; STXM fractional composition maps showing the concentration of (k) TQ1 and (l) N2200 with corresponding STXM mass plots (m and n) and (o) position-matched TEM for 2:1 TQ1:N2200 nanoparticles. All scale bars are 1 μm. The colour contrast is scaled such that light colours correspond to higher component concentrations. For the mass plots (c, d, h, i, m, n) the colour scale bars indicate concentration of component in mg cm^{-2}.

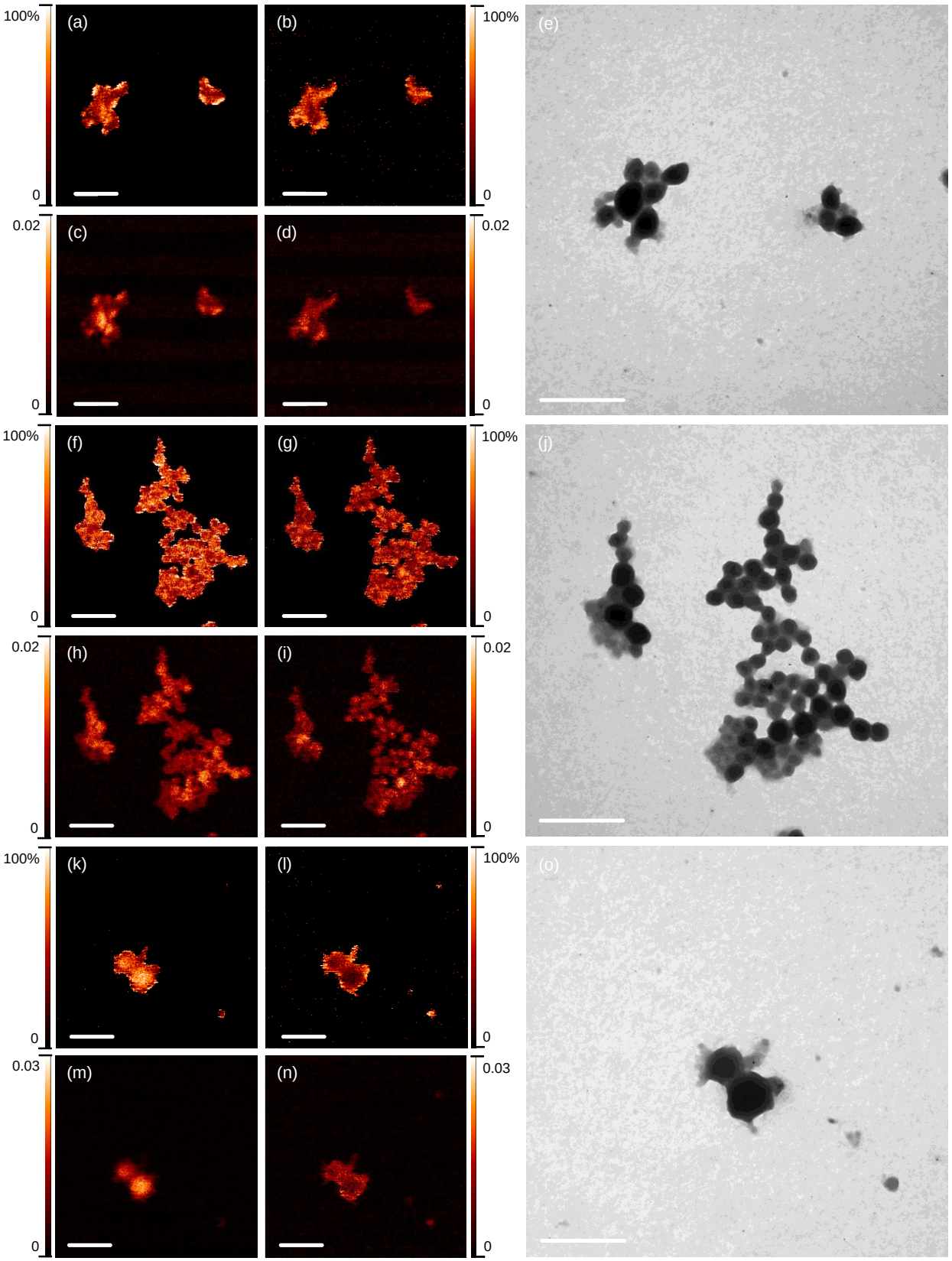

Figure 4. STXM fractional composition maps showing the concentration of (a) P3HT and (b) N2200 with corresponding STXM mass plots (c and d) and (e) position-matched TEM for 1:1 P3HT:N2200 nanoparticles;

STXM fractional composition maps showing the concentration of (f) P3HT and (g) o-IDTBR with corresponding STXM mass plots (h and i) and (j) position-matched TEM for 1:1 P3HT:o-IDTBR nanoparticles; STXM fractional composition maps showing the concentration of (k) P3HT and (l) eh-IDTBR with corresponding STXM mass plots (m and n) and (o) position-matched TEM for 1:1 P3HT:eh-IDTBR nanoparticles. All scale bars are 1 μm. The colour contrast is scaled such that light colours correspond to higher component concentrations. For the mass plots (c, d, h, i, m, n) the colour scale bars indicate concentration of component in mg cm^{-2}.

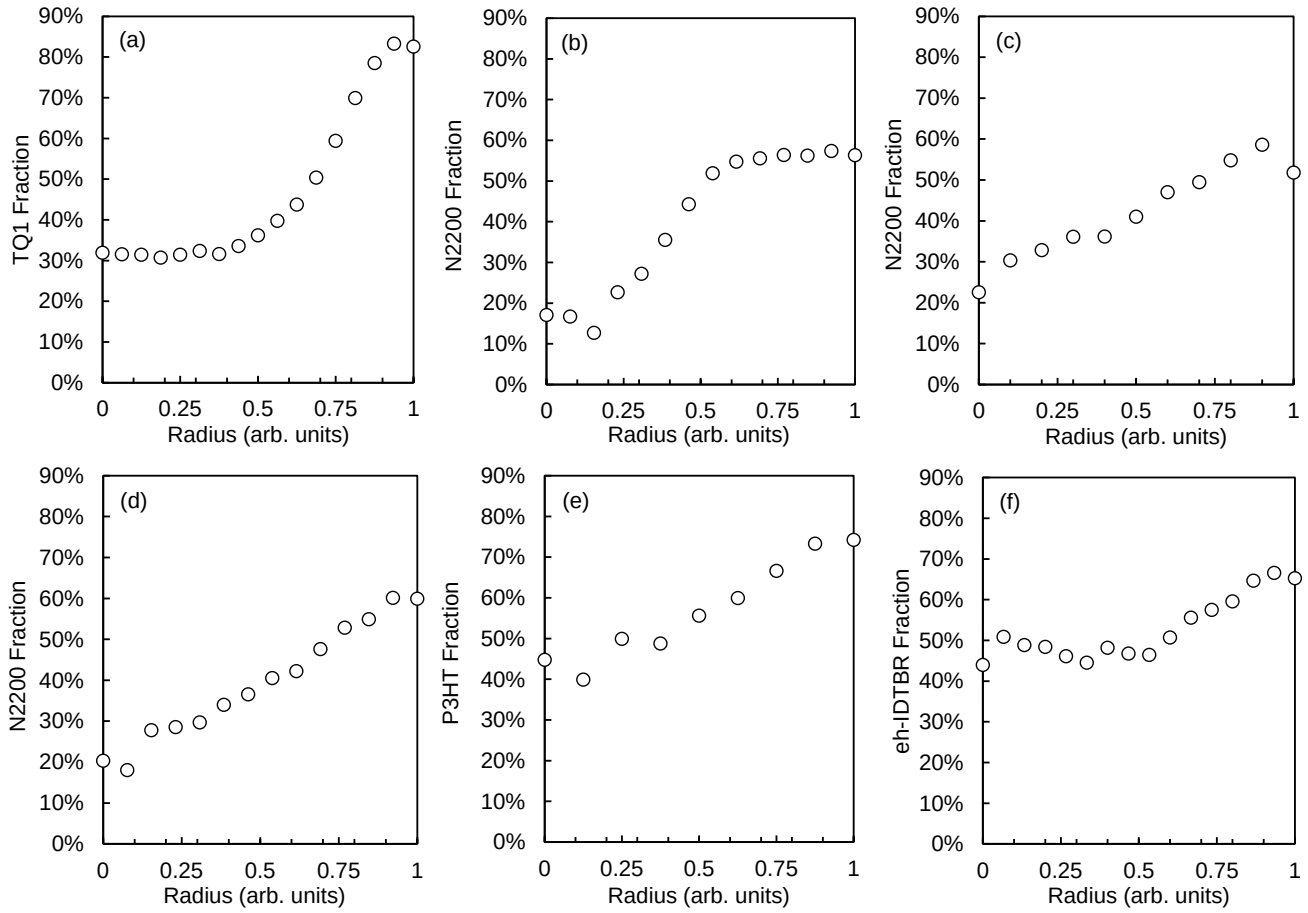

Figure 5. A typical radial profile of a nanoparticle synthesized for the material system (a) TQ1:PNDIT10 (1:1), (b) TQ1:N2200 (1:1), (c) TQ1:N2200 (2:1), (d) P3HT:N2200 (1:1), (e) P3HT:o-IDTBR (1:1), and (f) P3HT:eh-IDTBR (1:1). Radial profiles were extracted from STXM fractional composition maps. Each data point represents a spatial distance of 16 nm.

Table 3. Compositional analysis of donor-acceptor nanoparticles, as calculated from STXM maps.

Donor-Acceptor System	Morphology Classification	Nanoparticle Shell		Nanoparticle Core	
		Predominant Shell Component	Composition (%) (σ)	Predominant Core Component	Composition (%) (σ)
NFAs combined with TQ1 donor					
1:1 TQ1:PNDIT10	Core-shell (NFA core)	TQ1	TQ1: 80 (4) PNDIT10: 20 (4)	PNDIT10	TQ1: 16 (9) PNDIT10: 84 (9)
1:1 TQ1:N2200	Core-shell (NFA shell)	N2200	TQ1: 45 (3) N2200: 55 (3) [e]	TQ1	TQ1: 92 (5) N2200: 8 (5)
2:1 TQ1:N2200	Core-shell (NFA shell)	N2200	TQ1: 47 (5) N2200: 53 (5) [e]	TQ1	TQ1: 87 (9) N2200: 13 (9)
NFAs combined with P3HT donor					
1:1 P3HT:N2200	Core-shell (NFA shell)	N2200	P3HT: 39 (7) N2200: 61 (7) [e]	P3HT	P3HT: 91 (6) N2200: 9 (6)
1:1 P3HT:o-IDTBR	Core-shell (NFA core)	P3HT	P3HT: 69 (6) o-IDTBR: 31 (6)	o-IDTBR	P3HT: 26 (16) o-IDTBR: 74 (16)
1:1 P3HT:eh-IDTBR	Core-shell (NFA shell)	eh-IDTBR	P3HT: 29 (6) eh-IDTBR: 71 (6)	P3HT	P3HT: 61 (7) eh-IDTBR: 39 (7)

[e] While the TQ1:N2200 and P3HT:N2200 nanoparticles contain N2200-rich shells, the absolute N2200 content of these nanoparticles is a small fraction lower than expected, being due to the low solubility of the high molecular weight polymer batch (M_n 150,500 Da) in solvent. The low solubility of the high molecular weight N2200 batch also accounts for the minimal change in domain composition when the ratio of TQ1 to N2200 changes (and hence N2200 loading changes) when moving from the 2:1 sample to the 1:1 sample.

Correlation of Surface Energy to Morphology

Previous studies of fullerene-containing systems have shown that the surface energy of different components in both bulk heterojunction blends[67,68] and binary nanoparticles[36] determines their segregation and location in the blend system. Although surface energy – morphology correlations have been commonly reported in the BHJ literature for many years, such a correlation has not been thoroughly investigated for nanoparticulate structures with a material sample set greater than two. And the BHJ system differs substantially to the nanoparticulate system, where the thermodynamics of the latter are complicated by the additional morphology consideration of kinetically stabilized waterborne nanoparticle formation. The core-shell formation reported in this study can be correlated to the relative surface energies of the donor and acceptor materials (listed in Table 1), where to minimize total energy the material with the lower surface energy migrates to the outer surface of the miniemulsion droplets during organic solvent evaporation and nanoparticle formation. For the TQ1:PNDIT10 nanoparticles, we observe a TQ1-rich shell and PNDIT10-rich core structure, as the surface energy of PNDIT10 is 30.1 mJ m^{-2} which is higher than that of TQ1 at 29 mJ m^{-2}. For both the 1:1 and 2:1 w/w ratio TQ1:N2200 nanoparticles we observe a N2200-rich shell and TQ1-rich core, as TQ1 has a higher surface energy than

N2200 (23.7 mJ m^{-2}). Similarly, the P3HT:N2200 nanoparticles possess N2200-rich shells as the surface energy of P3HT (26.9 mJ m^{-2}) is also higher than that of N2200. For the IDTBR-based nanoparticles, a P3HT-rich shell and o-IDTBR-rich core is attributed to the higher surface energy of o-IDTBR (28.1 mJ m^{-2}) than P3HT, this structure then shifts to an eh-IDTBR-rich shell / P3HT-rich core for the P3HT:eh-IDTBR nanoparticles due to the lower surface energy of eh-IDTBR (18.3 mJ m^{-2}) relative to P3HT. A direct comparison can be made specifically to previous results reported for TQ1:fullerene[34] and P3HT:fullerene[29,35–37,69] systems, where the polymer donor occupies the nanoparticle shell for each case and the fullerene acceptor occupies the core.

Conceptual Model for Core-Shell Flipping

We observe a core-shell flipping driven by the low surface energy NFA N2200 (23.7 mJ m^{-2}) and eh-IDTBR (18.3 mJ m^{-2}) materials, where an inverted shell-core structure is the result of the NFA moving to the nanoparticle *shell*. A conceptual model illustrating this core-shell flipping driven by the relative surface energy of the donor and acceptor materials is presented in Figure 6. We also calculated the surface energy differential, $\Delta G_{surface}$, between components in the nanoparticle ($\Delta G = G_{surface(acceptor)} - G_{surface(donor)}$), plotting the relationship between nanoparticle shell composition and the surface energy differential in Figure 7, with tabulated data provided in Table 4. A linear correlation is observed between these two parameters, with the shell dominated by the material with the lower surface energy. In addition, we have plotted data points from our prior work reporting P3HT:$PC_{61}BM$ and TQ1:$PC_{71}BM$ nanoparticles, finding that they are consistent with the trend line from the NFA materials. This result indicates that the surface energy nanoengineering approach provides consistent results across multiple different materials systems. A distinct comparison can be observed between the morphology of donor:NFA nanoparticles and donor:fullerene acceptor nanoparticles. Due to the exceptionally high surface energy of the fullerene acceptors ($PC_{61}BM$ = 38.2 mJ cm^{-2}; $PC_{71}BM$ = 39 mJ m^{-2}), synthetic flexibility is lost and the fullerene becomes strongly localized in the binary nanoparticle *core* regardless of the donor polymer.[34,36] In contrast, our results show that inverted shell-core structured nanoparticles are now possible when using NFAs that are no longer pinned to such high surface energies, with the NFAs spanning a range of surface energies great enough to tune the nanoparticle shell composition between 20 and 70%. The ability to span a range of $\Delta G_{surface}$ values from positive to negative highlights that these NFA materials offer sophisticated control over internal nanoparticle morphology.

Table 4. Tabulated nanoparticle shell composition and surface energy differential for donor:NFA and donor:fullerene acceptor systems.

Donor-Acceptor System	**Acceptor Composition in Nanoparticle Shell (%)**	**$\Delta G_{surface}$ ($G_{surface(acceptor)}$ - $G_{surface(donor)}$) (mJ m^{-2})**
NFA acceptor		
TQ1:PNDIT10	20 (4)	1.1
TQ1:N2200	55 (3)	-5.3
P3HT:N2200	61 (7)	-3.2
P3HT:o-IDTBR	31 (6)	1.2
P3HT:eh-IDTBR	71 (6)	-8.6
Fullerene acceptor (for comparison purposes)		
P3HT:$PC_{61}BM$	30 (1) [37]	11.3
TQ1:$PC_{71}BM$	22.5 (8) [34]	10

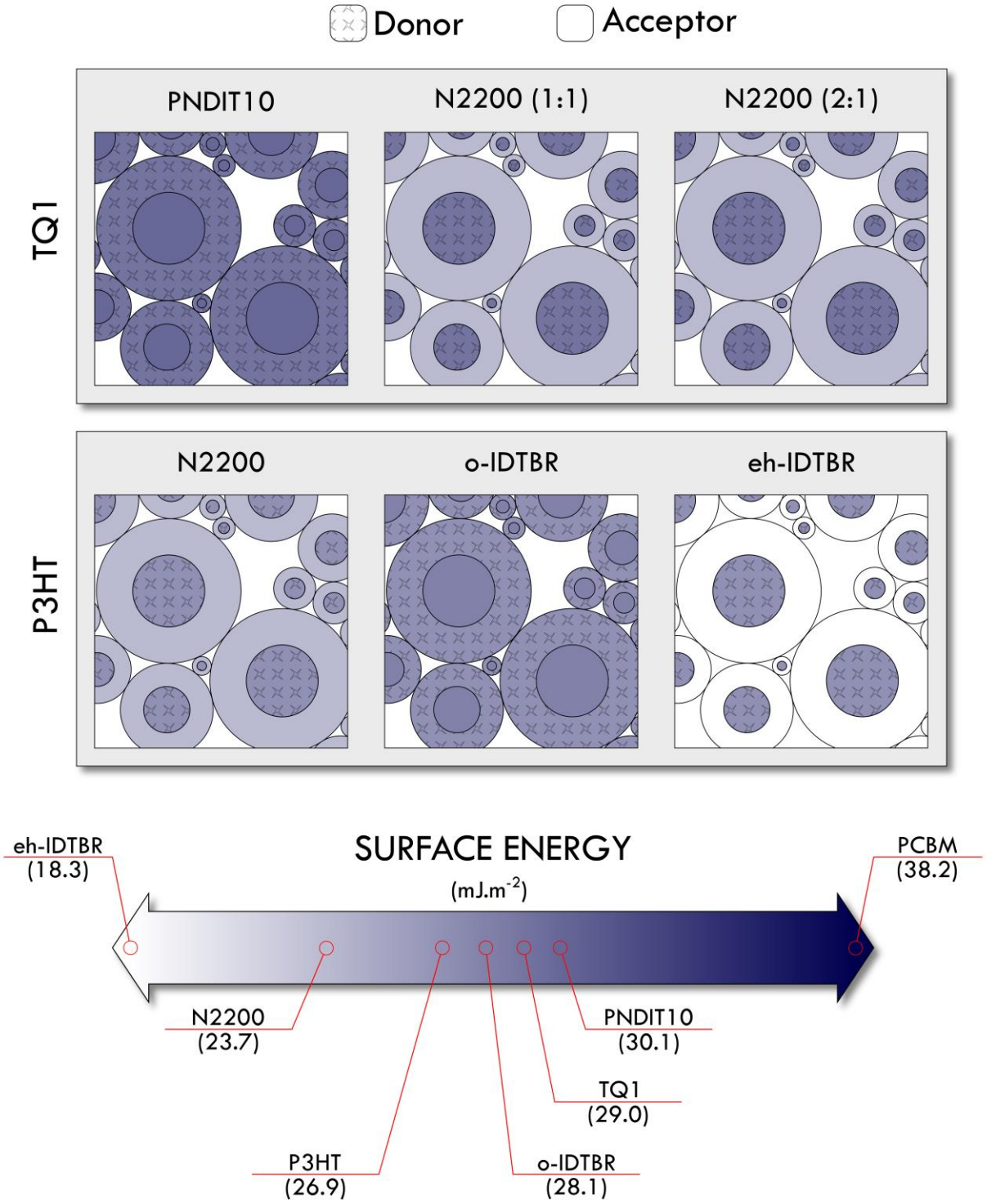

Figure 6. Conceptual schematic incorporating core-shell structure observed for each donor-acceptor system, depicting the correlation between material surface energy and nanoparticle morphology.

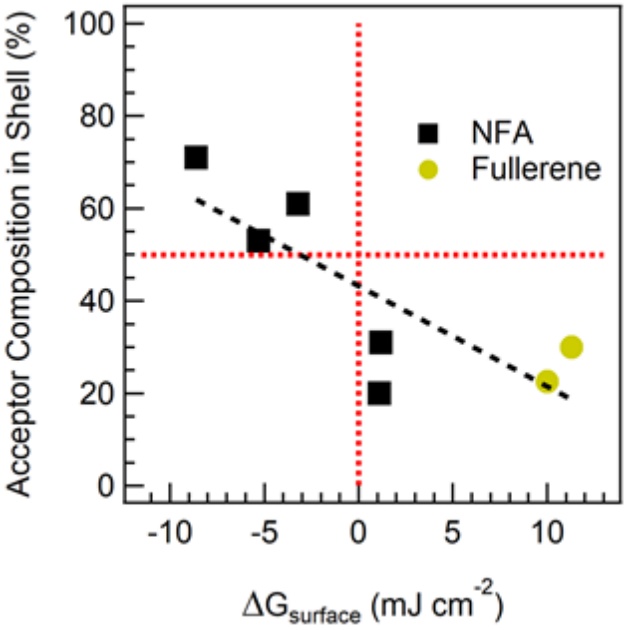

Figure 7. Relationship between nanoparticle shell composition and surface energy differential.

Outlook for Engineered Nanostructures

Here we establish a new figure of merit (FoM) for customizing the morphology of waterborne nanoparticulate colloidal inks, *surface energy*. With a $\triangle G_{surface} > 0$ yielding an acceptor core - donor shell structure, a $\triangle G_{surface} < 0$ yielding a donor core - acceptor shell structure (both determined empirically in this study), and a $\triangle G_{surface} = 0$ leading to a molecularly intermixed structure (hypothesized from this work). Interestingly, even small values of $\triangle G_{surface}$ of ~1 mJ cm^{-2} led to a phase separated core-shell structure for systems TQ1:PNDIT10 and P3HT:o-IDTBR. It is possible that for such small differences in the surface energy of the donor and acceptor materials, the morphology is also influenced by other factors, such as the nature of the surfactant. Indeed, Kosco et al.[41] showed that when utilizing SDS surfactant, core-shell structure can be obtained for large chloroform/water surface tension differences between the donor containing chloroform phase and the acceptor.

Incorporation of NFAs into waterborne donor-acceptor nanoparticles has shown great promise in tuning the structure of nanoparticles due to the large surface energy variation possible with NFA materials in comparison to their fullerene counterparts. We have shown that matched surface energies of donor and acceptor materials is a viable strategy for targeting a molecularly intermixed nanoparticle structure, which is an important challenge for optimizing organic nanoparticles for highly efficient eco-friendly organic photovoltaics. This matching of surface energies could be achieved by synthetic modification of

the NFA side chain chemistry in a systematic fashion in order to reach a desired target surface energy value for both acceptor and donor materials.

Conclusion

Here we report the acceptor core - donor shell *and* donor core - acceptor shell nanostructure formation of waterborne donor-acceptor nanoparticles via *self-assembly*, driven by the surface energy of the NFA relative to the donor organic semiconductor material. During nanoparticle formation, to lower the energy of the free surface the higher surface energy material of the two materials is driven to the nanoparticle core, and the lower surface energy material to the nanoparticle shell. We observed a core-shell flipping driven by the low surface energy NFA N2200 (23.7 mJ m^{-2}) and eh-IDTBR (18.3 mJ m^{-2}) materials, where an inverted shell-core structure was the result of the NFA moving to the nanoparticle *shell*. Customized waterborne nanoparticulate colloidal inks can be achieved by selecting donor and acceptor materials with a known surface energy differential. Furthermore, a highly promising strategy for generating intermixed donor-acceptor nanoparticles (as opposed to core-shell structured nanoparticles) is modification of the material surface energies via synthetic modification of a semiconductor's side chain chemistry to obtain matched surface energies for donor and acceptor, eliminating the drive for phase separation in the particle formation process. This morphology strategy has the goal of targeting nanostructured blends which promote efficient exciton dissociation and charge transport. The results of this study position surface energy to be a material property of equal importance to the existing key properties of organic semiconductors, namely, HOMO, LUMO, E_g and λ_{max}, for waterborne colloidal nanoparticles of organic semiconductors. We predict future studies of nanoparticle OPV will now involve five key criteria for the selection of suitable donor and acceptor materials, HOMO, LUMO, E_g, λ_{max} and surface energy.

Conflicts of Interest

There are no conflicts of interest to declare.

Acknowledgements

This research used resources of the Advanced Light Source, which is a DOE Office of Science User Facility under contract no. DE-AC02-05CH11231. The authors thank support staff at the Advanced Light Source synchrotron. We acknowledge travel funding provided by the International Synchrotron Access Program (ISAP) managed by the Australian Synchrotron, part of ANSTO, and funded by the Australian

Government. Thank you to Dr Katharina Witte and Dr Benjamin Watts for NEXAFS measurements of eh-IDTBR at the Swiss Light Source, PolLux beamline. The PolLux endstation was financed by the BMBF through contracts 05K16WED and 05K19WE2. This work was performed in part at the Materials Node (Newcastle) of the Australian National Fabrication Facility (ANFF), which is a company established under the National Collaborative Research Infrastructure Strategy to provide nano- and microfabrication facilities for Australia's researchers. Thank you to the University of Newcastle Electron Microscopy and X-ray (EMX) Unit for providing access to electron microscopes. TWJ thanks the CSIRO Energy Business Unit for funding. Finally, we would like to thank Philippe Legros, CNRS Engineer at PLACAMAT UMS3626, CNRS-Univ. Bordeaux, 33600 PESSAC-FRANCE, for the preliminary SEM analysis and Robin Szymanski for providing UV-visible spectra of o- and eh-IDTBR.

Supplementary Material

Supporting material for this article is available online.

References

(1) Zhong, Y.; Yin, L.; He, P.; Liu, W.; Wu, Z.; Wang, H. Surface Chemistry in Cobalt Phosphide-Stabilized Lithium − Sulfur Batteries. *J. Am. Chem. Soc.* **2018**, *140*, 1455–1459.

(2) Newton, J. E.; Preece, J. A.; Rees, N. V; Horswell, S. L. Nanoparticle Catalysts for Proton Exchange Membrane Fuel Cells : Can Surfactant Effects Be Beneficial for Electrocatalysis ? *Phys. Chem. Che* **2014**, *16*, 11435–11446.

(3) Campisi, S.; Schiavoni, M.; Chan-thaw, C. E.; Villa, A. Untangling the Role of the Capping Agent in Nanocatalysis: Recent Advances and Perspectives. *Catalysts* **2016**, *6* (12), 185.

(4) Chang, M.; Reichmanis, E. An Approach to Core-Shell Nanostructured Materials with High Colloidal and Chemical Stability: Synthesis, Characterization and Mechanistic Evaluation. *Colloid Polym. Sci.* **2012**, *290* (18), 1913–1926.

(5) Bau, J. A.; Luber, E. J.; Buriak, J. M. Oxygen Evolution Catalyzed by Nickel-Iron Oxide Nanocrystals with a Nonequilibrium Phase. *ACS Appl. Mater. Interfaces* **2015**, *7* (35), 19755–19763.

(6) Green, M. The Nature of Quantum Dot Capping Ligands. *J. Mater. Chem.* **2010**, *20*, 5797–5809.

(7) Giansante, C.; Infante, I. Surface Traps in Colloidal Quantum Dots: A Combined Experimental and Theoretical Perspective. *J. Phys. Chem. Lett.* **2017**, *8*, 5209–5215.

(8) Goldmann, C.; Lazzari, R.; Paquez, X.; Boissiere, C.; Ribot, F.; Sanchez, C.; Chane, C.; Portehault, D. Charge Transfer at Hybrid Interfaces: Plasmonics of Aromatic Thiol-Capped. *ACS Nano* **2015**, *9* (7), 7572–7582.

(9) Li, N.; Zhao, P.; Astruc, D. Anisotrope Gold-Nanopartikel: Synthese, Eigenschaften, Anwendungen Und Toxizitat. *Angew. Chemie* **2014**, *126*, 1784–1818.

(10) Bardhan, R.; Lal, S.; Joshi, A.; Halas, N. J. Theranostic Nanoshells: From Probe Design to Imaging and Treatment of Cancer. *Acc. Chem. Res.* **2011**, *44* (10), 936–946.

(11) Shipway, A. N.; Katz, E.; Willner, I. Nanoparticle Arrays on Surfaces for Electronic, Optical, and Sensor Applications. *ChemPhysChem* **2000**, *1*, 18–52.

(12) Bau, J. A.; Li, P.; Marenco, A. J.; Trudel, S.; Olsen, B. C.; Luber, E. J.; Buriak, J. M. Nickel/Iron Oxide Nanocrystals with a Nonequilibrium Phase: Controlling Size, Shape, and Composition. *Chem. Mater.* **2014**, *26* (16), 4796–4804.

(13) Feldheim, D. L.; Keating, C. D. Self-Assembly of Single Electron Transistors and Related Devices. *Chem. Soc. Rev.* **1998**, *27*, 1–12.

(14) Gärtner, S.; Christmann, M.; Sankaran, S.; Röhm, H.; Prinz, E.-M.; Penth, F.; Pütz, A.; Türeli, A. E.; Penth, B.; Baumstümmler, B.; et al. Eco-Friendly Fabrication of 4% Efficient Organic Solar Cells from Surfactant-Free P3HT:ICBA Nanoparticle Dispersions. *Adv. Mater.* **2014**, *26*, 6653–6657.

(15) Xie, C.; Heumüller, T.; Gruber, W.; Tang, X.; Classen, A.; Schuldes, I.; Bidwell, M.; Späth, A.; Fink, R. H.; Unruh, T.; et al. Overcoming Efficiency and Stability Limits in Water-Processing Nanoparticular Organic Photovoltaics by Minimizing Microstructure Defects. *Nat. Commun.* **2018**, *9*, 5335.

(16) Lee, Y.; Choi, J.; Lee, K. J.; Stott, N. E. Large-Scale Synthesis of Copper Nanoparticles by Chemically Controlled Reduction for Applications of Inkjet-Printed Electronics. *Nanotechnology* **2008**, *19*, 415604.

(17) Yang, Z.; Wei, J.; Sobolev, Y. I.; Grzybowski, B. A. Systems of Mechanized and Reactive Droplets Powered by Multi-Responsive Surfactants. *Nature* **2018**, *553*, 313–318.

(18) Chu, Z.; Peng, J.; Jin, W. Advanced Nanomaterial Inks for Screen-Printed Chemical Sensors. *Sensors Actuators B. Chem.* **2017**, *243*, 919–926.

(19) Grubbs, R. B. Roles of Polymer Ligands in Nanoparticle Stabilization Roles of Polymer Ligands in Nanoparticle Stabilization. *Polym. Rev.* **2007**, *47*, 197–215.

(20) Persson, N. E.; Chu, P. H.; McBride, M.; Grover, M.; Reichmanis, E. Nucleation, Growth, and Alignment of Poly(3-Hexylthiophene) Nanofibers for High-Performance OFETs. *Acc. Chem. Res.* **2017**, *50* (4), 932–942.

(21) Holliday, S.; Ashraf, R. S.; Wadsworth, A.; Baran, D.; Yousaf, S. A.; Nielsen, C. B.; Tan, C. H.; Dimitrov, S. D.; Shang, Z.; Gasparini, N.; et al. High-Efficiency and Air-Stable P3HT-Based Polymer Solar Cells with a New Non-Fullerene Acceptor. *Nat. Commun.* **2016**, *7*, 11585.

(22) Li, Z.; Xu, X.; Zhang, W.; Meng, X.; Ma, W.; Yartsev, A.; Inganäs, O.; Andersson, M. R.; Janssen, R. A. J.; Wang, E. High Performance All-Polymer Solar Cells by Synergistic Effects of

Fine-Tuned Crystallinity and Solvent Annealing. *J. Am. Chem. Soc.* **2016**, *138*, 10935–10944.

(23) Liu, Q.; Jiang, Y.; Jin, K.; Qin, J.; Xu, J.; Li, W.; Xiong, J.; Liu, J.; Xiao, Z.; Sun, K.; et al. 18% Efficiency Organic Solar Cells. *Sci. Bull.* **2020**, *65* (4), 272–275.

(24) Sun, H.; Liu, T.; Yu, J.; Lau, T.-K.; Zhang, G.; Zhang, Y.; Su, M.; Tang, Y.; Ma, R.; Liu, B.; et al. A Monothiophene Unit Incorporating Both Fluoro and Ester Substitution Enabling High-Performance Donor Polymers for Non-Fullerene Solar Cells with 16.4% Efficiency. *Energy Environ. Sci.* **2019**, *12*, 3328–3337.

(25) Espinosa, N.; García-Valverde, R.; Urbina, A.; Krebs, F. C. A Life Cycle Analysis of Polymer Solar Cell Modules Prepared Using Roll-to-Roll Methods Under Ambient Conditions. *Sol. Energy Mater. Sol. Cells* **2011**, *95* (5), 1293–1302.

(26) Landfester, K.; Montenegro, R.; Scherf, U.; Güntner, R.; Asawapirom, U.; Patil, S.; Neher, D.; Kietzke, T. Semiconducting Polymer Nanospheres in Aqueous Dispersion Prepared by a Miniemulsion Process. *Adv. Mater.* **2002**, *14* (9), 651–655.

(27) Kietzke, T.; Neher, D.; Landfester, K.; Montenegro, R.; Güntner, R.; Scherf, U. Novel Approaches to Polymer Blends Based on Polymer Nanoparticles. *Nat. Mater.* **2003**, *2* (6), 408–412.

(28) Kietzke, T.; Neher, D.; Kumke, M.; Montenegro, R.; Landfester, K.; Scherf, U. A Nanoparticle Approach to Control the Phase Separation in Polyfluorene Photovoltaic Devices. *Macromolecules* **2004**, *37* (13), 4882–4890.

(29) Ulum, S.; Holmes, N.; Barr, M.; Kilcoyne, A. L. D.; Gong, B. Bin; Zhou, X.; Belcher, W.; Dastoor, P. The Role of Miscibility in Polymer:Fullerene Nanoparticulate Organic Photovoltaic Devices. *Nano Energy* **2013**, *2*, 897–905.

(30) D'Olieslaeger, L.; Pirotte, G.; Cardinaletti, I.; D'Haen, J.; Manca, J.; Vanderzande, D.; Maes, W.; Ethirajan, A. Eco-Friendly Fabrication of PBDTTPD:PC71BM Solar Cells Reaching a PCE of 3.8% Using Water-Based Nanoparticle Dispersions. *Org. Electron. physics, Mater. Appl.* **2017**, *42*, 42–46.

(31) Aubry, J.; Ganachaud, F.; Addad, J.-P. C.; Cabane, B. Nanoprecipitation of Polymethylmethacrylate by Solvent Shifting: 1. Boundaries. *Langmuir* **2009**, *25* (4), 1970–1979.

(32) Xia, Y.; Musumeci, C.; Bergqvist, J.; Ma, W.; Gao, F.; Tang, Z.; Bai, S.; Jin, Y.; Zhu, C.; Kroon, R.; et al. Inverted All-Polymer Solar Cells Based on a Quinoxaline-Thiophene/Naphthalene-Diimide Polymer Blend Improved by Annealing. *J. Mater. Chem. A* **2016**, *4* (10), 3835–3843.

(33) Dang, M. T.; Hirsch, L.; Wantz, G. P3HT:PCBM, Best Seller in Polymer Photovoltaic Research. *Adv. Mater.* **2011**, *23*, 3597–3602.

(34) Holmes, N. P.; Marks, M.; Kumar, P.; Kroon, R.; Barr, M. G.; Nicolaidis, N.; Feron, K.; Pivrikas, A.; Fahy, A.; Diaz De Zerio Mendaza, A.; et al. Nano-Pathways: Bridging the Divide between Water-Processable Nanoparticulate and Bulk Heterojunction Organic Photovoltaics.

Nano Energy **2016**, *19*, 495–510.

(35) Holmes, N. P.; Burke, K. B.; Sista, P.; Barr, M.; Magurudeniya, H. D.; Stefan, M. C.; Kilcoyne, A. L. D.; Zhou, X.; Dastoor, P. C.; Belcher, W. J. Nano-Domain Behaviour in P3HT:PCBM Nanoparticles, Relating Material Properties to Morphological Changes. *Sol. Energy Mater. Sol. Cells* **2013**, *117*, 437–445.

(36) Ulum, S.; Holmes, N.; Darwis, D.; Burke, K.; David Kilcoyne, A. L.; Zhou, X.; Belcher, W.; Dastoor, P. Determining the Structural Motif of P3HT:PCBM Nanoparticulate Organic Photovoltaic Devices. *Sol. Energy Mater. Sol. Cells* **2013**, *110*, 43–48.

(37) Holmes, N. P.; Nicolaidis, N.; Feron, K.; Barr, M.; Burke, K. B.; Al-Mudhaffer, M.; Sista, P.; Kilcoyne, A. L. D.; Stefan, M. C.; Zhou, X.; et al. Probing the Origin of Photocurrent in Nanoparticulate Organic Photovoltaics. *Sol. Energy Mater. Sol. Cells* **2015**, *140*, 412–421.

(38) Almyahi, F.; Andersen, T. R.; Cooling, N.; Holmes, N. P.; Fahy, A.; Barr, M. G.; Kilcoyne, D.; Belcher, W.; Dastoor, P. C. Optimization, Characterization and Upscaling of Aqueous Solar Nanoparticle Inks for Organic Photovoltaics Using Low-Cost Donor:Acceptor Blend. *Org. Electron.* **2018**, *52*, 71–78.

(39) Al-Mudhaffer, M. F.; Griffith, M. J.; Feron, K.; Nicolaidis, N. C.; Cooling, N. A.; Zhou, X.; Holdsworth, J.; Belcher, W. J.; Dastoor, P. C. The Origin of Performance Limitations in Miniemulsion Nanoparticulate Organic Photovoltaic Devices. *Sol. Energy Mater. Sol. Cells* **2018**, *175* (September 2017), 77–88.

(40) Subianto, S.; Balu, R.; Campo, L. De; Sokolova, A.; Dutta, N. K.; Choudhury, N. R.; Balu, R.; Campo, L. De; Sokolova, A.; Dutta, N. K.; et al. Sulfonated Thiophene Derivative Stabilized Aqueous Poly(3-Hexylthiophene):Phenyl-C61-Butyric Acid Methyl Ester Nanoparticle Dispersion for Organic Solar Cell Applications. *ACS Appl. Mater. Interfaces* **2018**, *10*, 44116–44125.

(41) Kosco, J.; Bidwell, M.; Cha, H.; Martin, T.; Howells, C. T.; Sachs, M.; Anjum, D. H.; Gonzalez Lopez, S.; Zou, L.; Wadsworth, A.; et al. Enhanced Photocatalytic Hydrogen Evolution from Organic Semiconductor Heterojunction Nanoparticles. *Nat. Mater.* **2020**, *19* (5), 559–565.

(42) Ma, Z.; Zhao, B.; Gong, Y.; Deng, J.; Tan, Z. Green-Solvent-Processable Strategies for Achieving Large-Scale Manufacture of Organic Photovoltaics. *J. Mater. Chem. A* **2019**, *7*, 22826–22847.

(43) Holmes, N. P.; Marks, M.; Cave, J. M.; Feron, K.; Barr, M. G.; Fahy, A.; Sharma, A.; Pan, X.; Kilcoyne, D. A. L.; Zhou, X.; et al. Engineering Two-Phase and Three-Phase Microstructures from Water-Based Dispersions of Nanoparticles for Eco-Friendly Polymer Solar Cell Applications. *Chem. Mater.* **2018**, *30*, 6521−6531.

(44) Wang, E.; Hou, L.; Wang, Z.; Hellström, S.; Zhang, F.; Inganäs, O.; Andersson, M. R. An Easily Synthesized Blue Polymer for High-Performance Polymer Solar Cells. *Adv. Mater.* **2010**, *22* (46), 5240–5244.

(45) Kilcoyne, A. L. D.; Tyliszczak, T.; Steele, W. F.; Fakra, S.; Hitchcock, P.; Franck, K.;

Anderson, E.; Harteneck, B.; Rightor, E. G.; Mitchell, G. E.; et al. Interferometer-Controlled Scanning Transmission X-Ray Microscopes at the Advanced Light Source. *J. Synchrotron Radiat.* **2003**, *10*, 125–136.

(46) Hansson, R.; Ericsson, L. K. E.; Holmes, N. P.; Rysz, J.; Opitz, A.; Campoy-Quiles, M.; Wang, E.; Barr, M. G.; Kilcoyne, A. L. D.; Zhou, X.; et al. Vertical and Lateral Morphology Effects on Solar Cell Performance for a Thiophene–Quinoxaline Copolymer:PC70BM Blend. *J. Mater. Chem. A* **2015**, *3*, 6970–6979.

(47) Wang, X.; Ederth, T.; Inganas, O. In Situ Wilhelmy Balance Surface Energy Determination of Poly(3-Hexylthiophene) and Poly(3,4-Ethylenedioxythiophene) during Electrochemical Doping-Dedoping. *Langmuir* **2006**, *22*, 9287–9294.

(48) Wang, S.; Fabiano, S.; Himmelberger, S.; Puzinas, S.; Crispin, X.; Salleo, A.; Berggren, M. Experimental Evidence That Short-Range Intermolecular Aggregation Is Sufficient for Efficient Charge Transport in Conjugated Polymers. *Proc. Natl. Acad. Sci. U. S. A.* **2015**, *112* (34), 10599–10604.

(49) Fabiano, S.; Himmelberger, S.; Drees, M.; Chen, Z.; Altamimi, R. M.; Salleo, A.; Loi, M. A.; Facchetti, A. Charge Transport Orthogonality in All-Polymer Blend Transistors, Diodes, and Solar Cells. *Adv. Energy Mater.* **2014**, *4*, 1301409.

(50) Liang, Q.; Jiao, X.; Yan, Y.; Xie, Z.; Lu, G.; Liu, J.; Han, Y. Separating Crystallization Process of P3HT and O-IDTBR to Construct Highly Crystalline Interpenetrating Network with Optimized Vertical Phase Separation. *Adv. Funct. Mater.* **2019**, *29* (47), 1807591.

(51) Krishnan Jagadamma, L.; Taylor, R. G. D.; Kanibolotsky, A. L.; Sajjad, M. T.; Wright, I. A.; Horton, P. N.; Coles, S. J.; Samuel, I. D. W.; Skabara, P. J. Highly Efficient Fullerene and Non-Fullerene Based Ternary Organic Solar Cells Incorporating a New Tetrathiocin-Cored Semiconductor. *Sustain. Energy Fuels* **2019**, *3* (8), 2087–2099.

(52) Fowkes, F. M. Attractive Forces at Interfaces. *Ind. Eng. Chem.* **1964**, *56* (12), 40–52.

(53) Chen, H. W.; Huang, T. Y.; Chang, T. H.; Sanehira, Y.; Kung, C. W.; Chu, C. W.; Ikegami, M.; Miyasaka, T.; Ho, K. C. Efficiency Enhancement of Hybrid Perovskite Solar Cells with MEH-PPV Hole-Transporting Layers. *Sci. Rep.* **2016**, *6* (September), 1–9.

(54) Wadsworth, A.; Hamid, Z.; Bidwell, M.; Ashraf, R. S.; Khan, J. I.; Anjum, D. H.; Cendra, C.; Yan, J.; Rezasoltani, E.; Guilbert, A. A. Y.; et al. Progress in Poly (3-Hexylthiophene) Organic Solar Cells and the Influence of Its Molecular Weight on Device Performance. *Adv. Energy Mater.* **2018**, *8*, 1801001.

(55) Guan, Z. L.; Kim, J. B.; Wang, H.; Jaye, C.; Fischer, D. A.; Loo, Y. L.; Kahn, A. Direct Determination of the Electronic Structure of the Poly(3-Hexylthiophene):Phenyl-[6,6]-C61 Butyric Acid Methyl Ester Blend. *Org. Electron.* **2010**, *11* (11), 1779–1785.

(56) Nicolaidis, N. C.; Al-Mudhaffer, M. F.; Holdsworth, J.; Zhou, X.; Belcher, W. J.; Dastoor, P. C. The Contribution of Fullerene Photocurrent Generation to Organic Solar Cell Performance. *J. Phys. Chem. C* **2019**, *123*, 11950–11958.

(57) Björström, C. M.; Bernasik, A.; Rysz, J.; Budkowski, A.; Nilsson, S.; Svensson, M.; Andersson, M. R.; Magnusson, K. O.; Moons, E. Multilayer Formation in Spin-Coated Thin Films of Low-Bandgap Polyfluorene:PCBM Blends. *J. Phys. Condens. Matter* **2005**, *17* (50), L529–L534.

(58) Ratcliff, E. L.; Meyer, J.; Steirer, K. X.; Armstrong, N. R.; Olson, D.; Kahn, A. Energy Level Alignment in PCDTBT:PC70BM Solar Cells: Solution Processed NiOx for Improved Hole Collection and Efficiency. *Org. Electron.* **2012**, *13* (5), 744–749.

(59) Chen, T. A.; Wu, X.; Rieke, R. D. Regiocontrolled Synthesis of Poly(3-Alkylthiophenes) Mediated by Rieke Zinc: Their Characterization and Solid-State Properties. *J. Am. Chem. Soc.* **1995**, *117*, 233–244.

(60) Clark, J.; Silva, C.; Friend, R. H.; Spano, F. C. Role of Intermolecular Coupling in the Photophysics of Disordered Organic Semiconductors: Aggregate Emission in Regioregular Polythiophene. *Phys. Rev. Lett.* **2007**, *98*, 206406.

(61) Sharma, A.; Pan, X.; Campbell, J. A.; Andersson, M. R.; Lewis, D. A. Unravelling the Thermomechanical Properties of Bulk Heterojunction Blends in Polymer Solar Cells. *Macromolecules* **2017**, *50*, 3347–3354.

(62) Desmond, K. W.; Weeks, E. R. Random Close Packing of Disks and Spheres in Confined Geometries. *Phys. Rev. E Phys. Rev. E*, **2009**, *80*, 051305.

(63) Desmond, K. W.; Weeks, E. R. Influence of Particle Size Distribution on Random Close Packing of Spheres. *Phys. Rev. E - Stat. Nonlinear, Soft Matter Phys.* **2014**, *90* (2), 1–6.

(64) Stoeva, S. I.; Prasad, B. L. V.; Uma, S.; Stoimenov, P. K.; Zaikovski, V.; Sorensen, C. M.; Klabunde, K. J. Face-Centered Cubic and Hexagonal Closed-Packed Nanocrystal Superlattices of Gold Nanoparticles Prepared by Different Methods. *J. Phys. Chem. B* **2003**, *107* (30), 7441–7448.

(65) McNeill, C. R.; Watts, B.; Thomsen, L.; Belcher, W. J.; Greenham, N. C.; Dastoor, P. C. Nanoscale Quantitative Chemical Mapping of Conjugated Polymer Blends. *Nano Lett.* **2006**, *6*, 1202–1206.

(66) Hu, H.; Ye, L.; Ghasemi, M.; Balar, N.; Rech, J. J.; Stuard, S. J.; You, W.; O'Connor, B. T.; Ade, H. Highly Efficient, Stable, and Ductile Ternary Nonfullerene Organic Solar Cells from a Two-Donor Polymer Blend. *Adv. Mater.* **2019**, *31*, 1808279.

(67) Huang, J. H.; Hsiao, Y. S.; Richard, E.; Chen, C. C.; Chen, P.; Li, G.; Chu, C. W.; Yang, Y. The Investigation of Donor-Acceptor Compatibility in Bulk-Heterojunction Polymer Systems. *Appl. Phys. Lett.* **2013**, *103* (4), 043304.

(68) Holmes, N. P.; Munday, H.; Barr, M. G.; Thomsen, L.; Marcus, M. A.; Kilcoyne, A. L. D.; Fahy, A.; Stam, J. van; Dastoor, P. C.; Moons, E. Unravelling Donor-Acceptor Film Morphology Formation for Environmentally-Friendly OPV Ink Formulations. *Green Chem.* **2019**, *21*, 5090–5103.

(69) Almyahi, F.; Andersen, T. R.; Cooling, N.; Holmes, N. P.; Fahy, A.; Barr, M. G.; Kilcoyne, D.;

Belcher, W.; Dastoor, P. C. Optimization, Characterization and Upscaling of Aqueous Solar Nanoparticle Inks for Organic Photovoltaics Using Low-Cost Donor : Acceptor Blend. *Org. Electron.* **2018**, *52*, 71–78.

For Table of Contents Only